ARTICLE

Engineered SERS Substrates with Multiscale Signal Enhancement: Nanoparticle Cluster Arrays

Bo Yan,[†] Anupama Thubagere,[†] W. Ranjith Premasiri,[∥] Lawrence D. Ziegler,[†,∥] Luca Dal Negro,[‡,§,∥] and Björn M. Reinhard[†,∥,*]

[†]Department of Chemistry, [‡]Department of Electrical and Computer Engineering, [§]Materials Science Division, and [∥]The Photonics Center, Boston University, Boston, Massachusetts 02215

ABSTRACT Defined nanoparticle cluster arrays (NCAs) with total lateral dimensions of up to 25.4 μm × 25.4 μm have been fabricated on top of a 10 nm thin gold film using template-guided self-assembly. This approach provides precise control of the structural parameters in the arrays, allowing a systematic variation of the average number of nanoparticles in the clusters (n) and the edge-to-edge separation (Λ) between $1 < n < 20$ and $50 \text{ nm} \leq \Lambda \leq 1000$ nm, respectively. Investigations of the Rayleigh scattering spectra and surface-enhanced Raman scattering (SERS) signal intensities as a function of n and Λ reveal direct near-field coupling between the particles within individual clusters, whose strength increases with the cluster size (n) until it saturates at around $n = 4$. Our analysis shows that strong near-field interactions between individual clusters significantly affect the SERS signal enhancement for edge-to-edge separations $\Lambda < 200$ nm. The observed dependencies of the Raman signals on n and Λ indicate that NCAs support a multiscale signal enhancement which originates from simultaneous inter- and intracluster coupling and $|E|$-field enhancement. The NCAs provide strong and reproducible SERS signals not only from small molecules but also from whole bacterial cells, which enabled a rapid spectral discrimination between three tested bacteria species: *Escherichia coli*, *Bacillus cereus*, and *Staphylococcus aureus*.

KEYWORDS: nanoparticle cluster arrays · SERS · bacterial pathogen detection · template-guided self-assembly · nanofabrication · photonic-plasmonic resonances

The intensities and frequencies of vibrational transitions measured in Raman spectra provide unique chemical signatures of molecular species, but the sensitivity of Raman spectroscopy suffers from the relatively low cross section of inelastically scattered Raman photons. In 1977, Jeanmaire and Van Duyne demonstrated that the magnitude of Raman cross sections can be greatly enhanced when the Raman-active molecules are placed on or near a roughened noble metal surface.[1] Since then, a wide variety of substrates has been found to enable surface-enhanced Raman spectroscopy (SERS)[2] such as aggregated noble metal colloids,[3−5] anisotropic metal nanoparticles,[6] metal island films,[7,8] metal film over nanospheres,[9] particles grafted on silanized glasses,[10] regular holes in thin noble metal films,[11] and regular nanoparticle arrays[12−20] to name only a few. In general, traditional SERS substrates can be divided into two fundamental substrate classes: random and engineered[21] substrates. Random substrates, such as fractal nanoparticle agglomerates, can support localized dipole modes, which lead to high SERS signal enhancements.[22,23] However, the resonance wavelength, the precise locations of the spots of giant $|E|$-field enhancement—so-called hot spots—and the reproducibility of their enhancement factors are difficult to control in completely random structures. Another disadvantage specific to fractal nanoparticle aggregates is that their mass density, and therefore the hot-spot density, decreases with increasing fractal size.[24]

Challenging applications of SERS in single molecule spectroscopy[25,26] or whole organism fingerprinting[27−29] would greatly benefit from engineered SERS substrates with rational design criteria that generate high SERS enhancement reproducibly at spatially defined locations. Consequently, regular nanoparticle arrays and other nanofabricated SERS substrates, whose characteristic structural parameters can be accurately controlled, have recently attracted significant interest as SERS substrates with reproducible, large enhancement factors "by design".[21,30] The SERS enhancement in noble metal nanoparticle arrays depends on both the properties of the constitutive building blocks such as shape, size, roughness, composition, as well as the geometric characteristics of the whole array, such as interparticle separation, array size, and geometry.[14,15,30] In general, two separate electromagnetic regimes govern the collective response of periodic metal nanoparticle arrays: near and far-field

*Address correspondence to bmr@bu.edu.

Received for review December 4, 2008 and accepted April 01, 2009.

Published online April 8, 2009.
10.1021/nn800836f CCC: $40.75

coupling.[14,17−20,31] When the particles are separated by short distances, up to approximately $S = 1/k_0 = \lambda_0/2\pi$ (with k_0 and λ_0 being the free space wavenumber and wavelength, respectively), strong quasi-static near-field interactions dominate the response of the array. Consequently, localized modes with strongly enhanced local fields are excited. When the particles are separated by larger distances, far-field diffractive coupling between the particles becomes dominant.[20,32]

In the near-field coupling regime, the field enhancement and corresponding SERS intensity arising from periodic arrays of nanoparticles sharply increase with decreasing interparticle separation.[14] Both theoretical[33,34] and experimental studies[35,36] have shown that regions of large $|E|$-field enhancement are located in the junction between individual particles. The $|E|$-field enhancement in these spatially confined hot spots can be orders of magnitude larger than on the surface of individual particles. Due to the rapid decay of the field strength with interparticle separation[37−39] and the $|E|^4$ scaling of the SERS signal, very short interparticle separations are vital in order to maximize the Raman enhancement in the near-field coupling regime.[33] Ideally, the analyte molecules are placed in the junctions between nearly touching metal surfaces.[35]

It remains challenging to create junction plasmons at predefined locations with nanometer accuracy in current top-down fabrication methods, such as electron beam (e-beam) lithography.[12−20] The spatial resolution of e-beam lithography is limited by laterally scattered secondary electrons, which make it difficult to reproducibly fabricate arrays with interparticle separations of less than 10 nm. In order to overcome this limitation, an alternative approach is demonstrated here that can be used to engineer SERS substrates with nanoscale interparticle separations reliably. Template-guided chemical self-assembly[40−43] is used to create nanoparticle cluster arrays (NCAs) of defined size with nanoscale interparticle separations at predefined pattern locations. E-beam lithography is not used to directly generate plasmonic structures but instead to define binding sites on which chemically synthesized gold nanoparticles can assemble. Consequently, "hot" internanoparticle junctions at predefined locations in a regular array can be created, enabling the possibility to control and optimize both near- and far-field noble metal nanoparticle interactions.

The goals of this paper are to systematically characterize the optical scattering spectra and the Raman signal intensity enhancements of these NCAs as a function of cluster size n and cluster edge-to-edge separation Λ, to compare their performance with nonpatterned colloidal gold films and periodic two-dimensional nanodisc arrays, and to demonstrate their applicability for the spectral discrimination between different bacterial pathogens. Rapid bacterial diagnostics are vital for improving the treatment outcomes of serious infections and ensuring the appropriate use of antibiotic strategies. A SERS-based approach for bacterial detection and identification relies on signal amplification and thus offers several potential advantages over sample amplification based techniques like PCR, such as speed, reduced susceptibility to contamination problems, ease-of-use, and mixture resolution for rapid, specific, and sensitive bacterial diagnostics.[27,28,44] The key requirement for the success of this methodology is the production of SERS substrates with large and reproducible signal enhancement. In this study, we demonstrate that NCAs provide reproducible SERS spectra of different bacteria species including *Escherichia coli* (*E. coli*), *Bacillus cereus* (*B. cereus*), and *Staphylococcus aureus* (*S. aureus*) with sufficient quality for potential diagnostic applications.

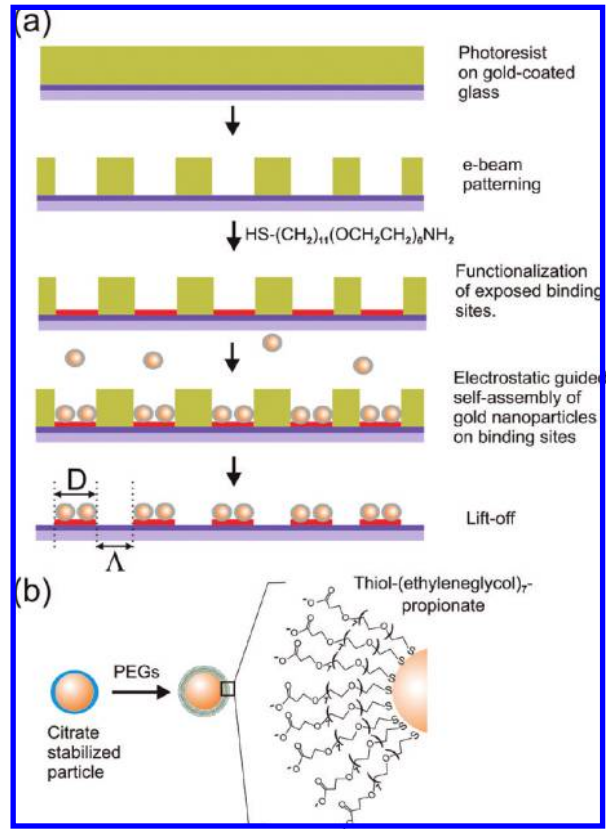

Figure 1. Template-assisted assembly of nanoparticle cluster arrays (NCAs). (a) Process flow of the template-assisted self-assembly. Electron beam (e-beam) lithography is used to define binding sites on which the dielectrically coated nanoparticles self-assemble. The characteristic array parameters *D* (binding site diameter) and Λ (cluster edge-to-edge separation) are indicated. (b) Assembly process uses 40 nm gold nanoparticles that are stabilized by a monolayer of short PEG molecules.

RESULTS AND DISCUSSION

Assembly of Regular Nanoparticle Cluster Arrays. The template-guided self-assembly strategy to generate regular two-dimensional arrays of contiguous nanoparticles is outlined in Figure 1a. In the first step, a regular structure of wells is created in a PMMA film on top of a 10 nm thin gold film using e-beam lithography. The re-

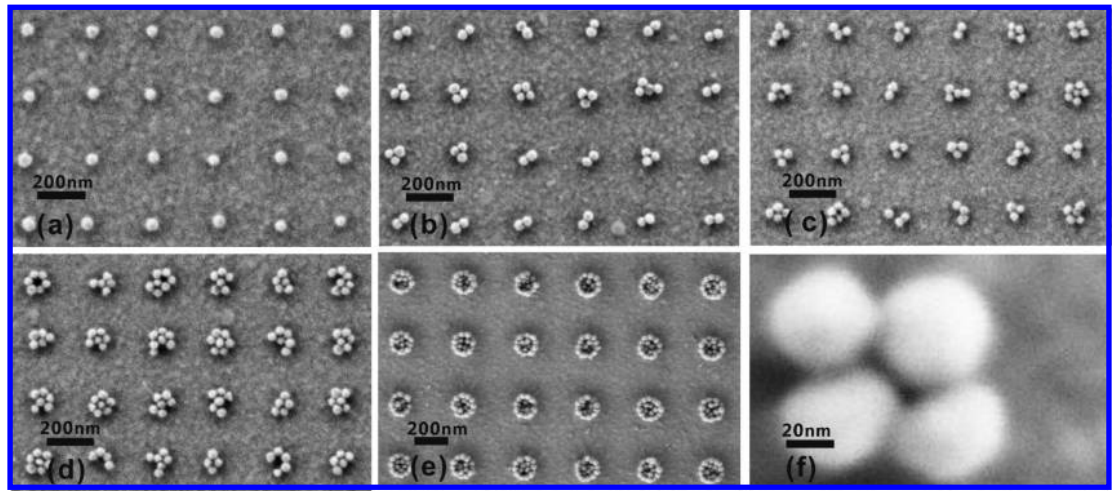

Figure 2. SEM images from extracts of nanoparticle cluster arrays with varying diameters of e-beam defined binding size D = 50 nm (a), 80 nm (b), 100 nm (c), 130 nm (d), 200 nm (e). The SEM images confirm that through control of the diameter of the e-beam fabricated binding site the cluster size can be continuously varied. The enlargement of an individual cluster in (f) shows junctions and crevices between nearly touching particles constituting a high degree of roughness on the nanoscale.

sulting PMMA mask covers all parts of the surface except for the anticipated binding sites. A monolayer of amino-terminated PEGs (thiol-$(CH2)_{11}EG_7$-amine, EG = ethyleneglycol) are assembled on the exposed gold surface. Under appropriate buffer conditions (pH <9), the monolayer is positively charged. Thus, negatively charged 40 nm colloidal gold nanoparticles readily bind on these positively charged binding sites in an electrostatic guided self-assembly process. The gold nanoparticles are passivated with a monolayer of carboxy-terminated PEGs (thiol-EG_7-propionat, see Figure 1b). The charged polymers on the gold surfaces serve two purposes; they facilitate an efficient charge-directed cluster assembly on the template and function as an insulating dielectric between the particles and between the nanoparticles and the gold support.

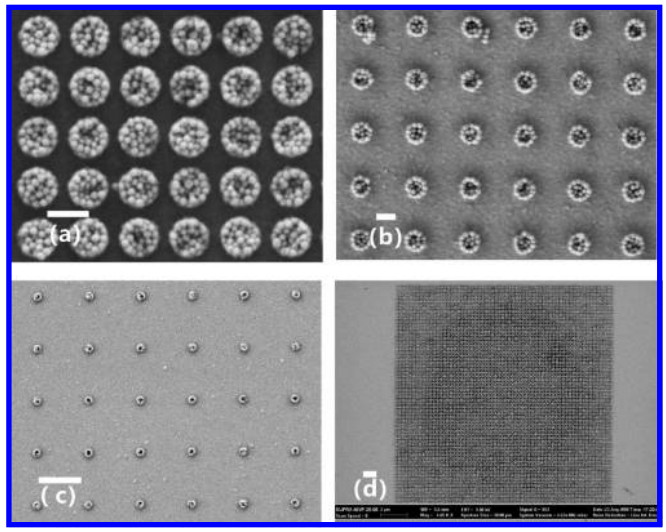

Figure 3. Extracts from nanoparticle cluster arrays with constant binding site diameter D = 200 nm but varying cluster edge-to-edge separations Λ = 50 nm (a), 200 nm (b), 1000 nm (c). In (d), the SEM of a complete array with D = 200 nm and Λ = 50 nm is shown. Scale bars in (a) and (b) are 200 nm; in (c) and (d) 1000 nm.

Scanning electron microscope (SEM) images of sections of the fabricated cluster arrays with the same edge-to-edge separation (Λ = 200 nm) but varying binding site diameters (D = 50, 80, 100, 130, 200 nm) are shown in Figure 2a−e. The SEM images show regular arrays of two-dimensional nanoparticle clusters with varying cluster size and confirm that the template-guided self-assembly approach leads to a spatially confined particle clustering into discrete assemblies. Figure 2 also shows that the average cluster size (*i.e.*, number of particles in the clusters) can be conveniently controlled by varying the binding site diameter D. For D = 50 nm, regular arrays of individual 40 nm gold nanoparticles with a high degree of translational symmetry are found. With increasing D, larger clusters are formed that exhibit some geometry and size variability. Even under ideal assembly conditions, a distribution of particle numbers and cluster geometry results from the natural size dispersion of the colloid used (coefficient of variation <20%). The low number of particles in the clusters makes the variation in the cluster size and shape most striking for intermediate binding sizes of D = 80 to 130 nm. In contrast, the larger clusters appear more homogeneous again.

Figure 2f shows an SEM of a particle clusters in the D = 80 nm NCA at higher magnification. As evident in this figure, the particle clusters contain holes, junctions, and crevices between few nanometer spaced gold nanoparticles. These nanoparticle gap structures are known to support a strong $|E|$-field localization, which can induce a strong enhancement of the dipole moment of the analyte molecules. The enhanced molecular dipole moments and the amplification of the re-radiated Raman scattered light through the noble metal

nanostructures lead to a strong enhancement of the SERS signal.[2]

To test the field enhancing effect of intercluster coupling, we also varied the cluster edge-to-edge separation Λ (see Figure 3). NCAs with $\Lambda = 50$, 100, 150, 200, 400, 600, 800, and 1000 nm and fixed binding site diameters between $D = 50$ and 200 nm were fabricated. It was difficult to decrease the edge-to-edge separation significantly below $\Lambda = 50$ nm, especially for larger cluster sizes, because at very short interparticle separations individual nanoparticle clusters fused and formed continuous lines of nanoparticle clusters across the pattern as shown in Figure S1 in the Supporting Information. Thus, the current template-assisted self-assembly approach can generate extended NCAs with a wide range of intercluster separations Λ and cluster sizes D, albeit with some limitation for the minimum intercluster separation. In the following, we will systematically analyze the optical response and the SERS enhancement as a function of Λ and D to obtain an understanding of the fundamental mechanisms governing the multilength scale electrodynamic interactions in NCAs.

Influence of the Cluster Edge-to-Edge Separation (Λ) on the Rayleigh Scattering Spectra of Nanoparticle Cluster Arrays. The optical response of dielectrically coated gold nanoparticles on a gold film is determined by the local plasmons of the particles, their interactions through space (near-field and far-field coupling),[19] and by their coupling to delocalized plasmon modes supported by the gold film.[45] The localized modes in the particles can couple with image modes in the gold film[46] as well as with plasmon modes in neighboring particles.[37] In addition, a gold surface which is periodically corrugated by gold nanoparticle clusters can act as a grating coupler.[47] In this case, photons incident on this surface can efficiently excite a propagating surface plasmon in the gold film, which can be Bragg-scattered from the regular cluster arrays.[47,48]

Given these different electromagnetic interactions between localized and delocalized plasmon modes in NCAs, it is challenging to quantitatively predict the optical response of the nanoparticle cluster arrays. As a first step toward an understanding of these potential SERS substrates, the spectral response of the NCAs was characterized as a function of the controllable template parameters Λ and D. To that end, we fabricated arrays with varying cluster edge-to-edge separations $\Lambda = 50-1000$ nm with a constant cluster binding size of $D = 200$ nm. The total area of the fabricated arrays varied from 25.4 μm $\times$ 25.4 μm for $\Lambda \geq 200$ nm to 16 μm $\times$ 16 μm for $\Lambda = 50$ nm. Due to the small size of the arrays, a spectral characterization of the arrays using extinction spectroscopy would be challenging. Instead, we decided to characterize the optical response of the NCAs using Rayleigh scattering spectroscopy, which can be conveniently performed in a darkfield microscope. With the help of a darkfield condenser, the excitation light can be injected into the specimen plane at such a steep angle from the bottom that only scattered light can reach the objective on top of the sample. The geometrical constraints of the darkfield illumination allow effective discrimination of the excitation light, and it is therefore an ideal technique for probing the plasmon resonances of nanostructures that do not provide a strong extinction.[17,19] Rayleigh scattering spectroscopy is routinely used to investigate the optical properties of a wide range of nanostructured plasmonic materials, including single noble metal nanoparticles,[49−51] regular one- and two-dimensional arrays of gold nanoparticles,[17] and deterministic aperiodic arrays of gold nanoparticles.[30]

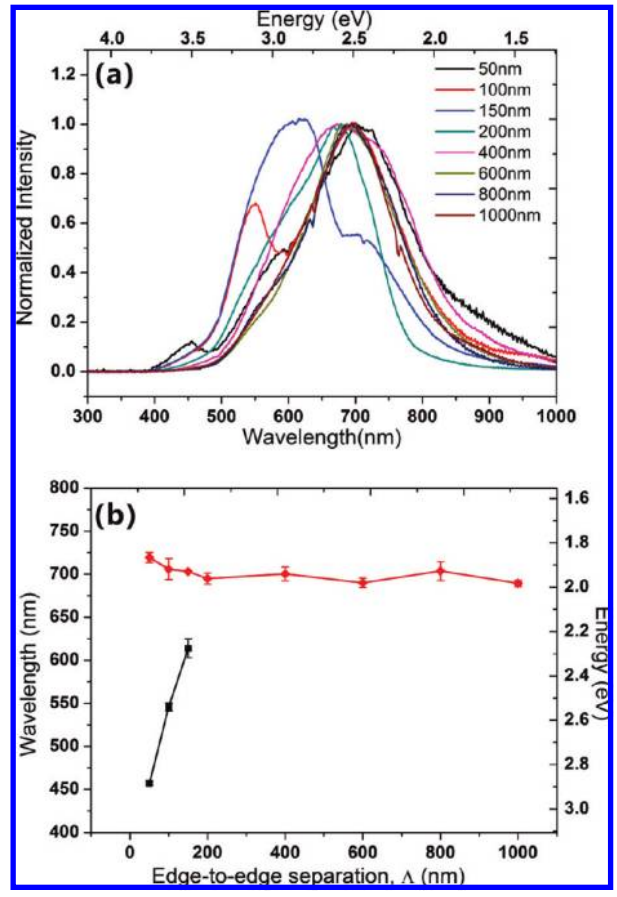

Figure 4. (a) Scattering spectra of NCAs with constant binding site diameter $D = 200$ nm as a function of the edge-to-edge separation Λ (see legend). (b) Fitted peak resonances as a function of Λ. The spectra of NCAs with $\Lambda < 200$ nm contain a short (black) and long (red) wavelength band. The short wavelength band arises from diffraction of the excitation light at the NCA. The long wavelength band is assigned to the plasmon resonance of the nanoparticle clusters on a gold support. The moderate blue shift of the long wavelength band with increasing separation between $\Lambda = 50$ and 200 nm indicates near-field interactions between the clusters in the arrays.

The normalized scattering spectra of the fabricated NCAs with varying Λ but fixed $D = 200$ nm are shown in Figure 4a. The displayed spectral intensities were not corrected by the different filling fractions of the arrays since we focus on the spectral shifts originating from differences in the array parameters in this study. All of

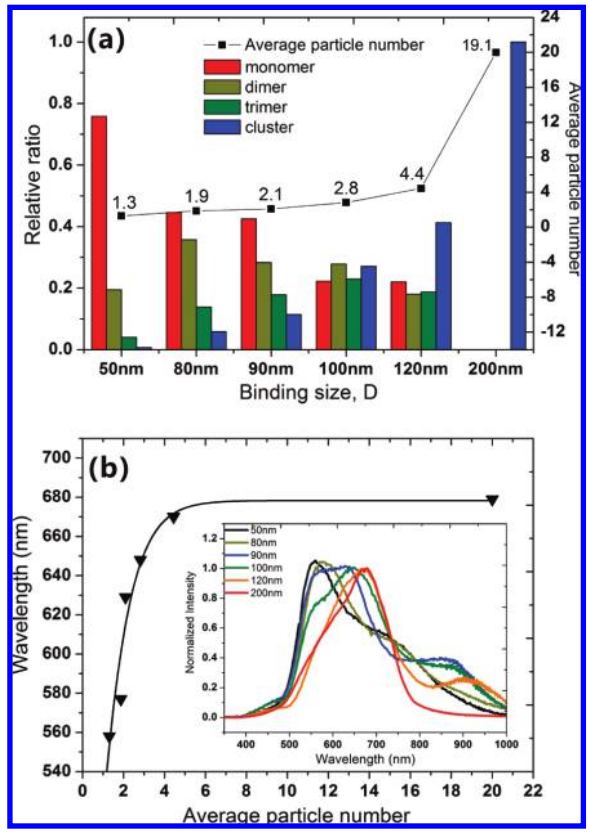

Figure 5. (a) Cluster size distribution and average cluster size *n* as function of the binding size *D*. (b) Dependency of the peak wavelength of NCAs with constant edge-to-edge separation Λ = 200 nm on the average cluster size *n*. The inset in (b) shows the original Rayleigh scattering spectra.

the spectra in Figure 4a show a broad peak around 700 nm, which we assign to the nanoparticle cluster resonance coupled *via* propagating surface plasmons in the gold support as described by Stuart *et al.*[52] and Felidj *et al.*[48] In addition to this coupled nanoparticle cluster resonance, NCAs with $\Lambda < 200$ nm exhibit a separate short wavelength band which strongly red shifts with increasing Λ. In Figure 4b, the fitted peak resonance wavelengths of these two bands are plotted as a function of Λ. The maximum of the short wavelength band shifts from ~455 nm (Λ = 50 nm) over ~545 nm (Λ = 100 nm) to ~613 nm (Λ = 150 nm). For $\Lambda \geq 200$ nm, a separate second peak can no longer be resolved. However, the spectrum of the NCA with Λ = 200 nm (Figure 4a) is asymmetrically broadened on the high energy side, indicating the possibility of additional spectral features.

Short wavelength bands next to the plasmon of the nanostructures have been observed previously in extinction measurements of regular arrays of smooth nanodiscs on gold. These features were ascribed to propagating surface plasmons or standing waves due to Bragg scattering from the nanoparticle array on top of the gold film.[48,53,54] These models have, however, only limited applicability to our scattering analysis because the investigated array geometries do not fulfill the grating coupling conditions[47] at our illumination angle (see below) in the investigated wavelength range. In addition, the correspondence between calculated Bragg scattering resonances and the measured high energy is approximate at best. Due to the experimental geometry of the performed scattering experiments, an alternative explanation for the short wavelength bands is that the periodic two-dimensional structure of gold nanoparticle clusters on top of the transparent 10 nm thin gold film acts like a transmission grating for some components of the incident light. Diffraction of the wavelength λ incident at angle ϕ_{inc} on the oil-immersed NCA is described by the grating formula:

$$L(\sin \varphi_{inc} + \sin \theta_{det}) = (m/n_r)\lambda \quad (1)$$

where L is the cluster center-to-center separation, θ_{det} is the detection angle, m is the diffraction order, and n_r is the refractive index of glass and index matching oil (n_r = 1.5).

The incident angle ϕ_{inc} is determined by the numerical aperture of the darkfield condenser. For a numerical aperture of NA = 1.2, ϕ_{inc} = 53°. The maximum detection angle θ_{det} is given by the marginal ray as determined by the objective numerical aperture. The numerical aperture of the objective used in these studies (NA = 0.65) results in a maximum θ_{det} = 25.7°. All wavelengths that fulfill eq 1 for $0° < \theta_{det} \leq 25.7°$ can be folded into the scattering spectrum. Following this model and considering the emission onset of the tungsten lamp at ~400 nm, peaks in the following spectral regions can be assigned to this diffraction effect: λ = 400−462 nm (Λ = 50 nm, L = 250 nm); λ = 400−555 nm (Λ = 100 nm, L = 300 nm); λ = 419−647 nm (Λ = 150 nm, L = 350 nm); λ = 479−754 nm (Λ = 200 nm, L = 400 nm). For larger Λ, the diffracted wavelengths are shifted out of the detection range. The experimentally observed short wavelength bands all fall in the wavelength ranges predicted by eq 1. We conclude that the simple transmission diffraction grating model suffices to explain the observed dependence of the high energy band on Λ.

The frequency of the lower energy band, assigned to the cluster plasmon resonance, appears to depend weakly on the cluster edge-to-edge separation Λ as shown in Figure 4b. This effect is, however, much smaller than that for the peak assigned to diffraction in the investigated Λ range. The cluster resonance peak (Figure 4b, red line) slightly blue shifts from 720 nm for Λ = 50 nm separations to 690 nm for Λ = 200 nm structures. At larger edge-to-edge distances, the cluster plasmon resonance peak does not appear to shift further. This small blue shift with increasing interparticle separation is attributed to direct near-field interactions between the clusters of the arrays on the gold substrate.[19]

Influence of Cluster Size on the Rayleigh Scattering Spectra of Nanoparticle Cluster Arrays. As evidenced in Figure 2, the average number of particles within the individual building blocks of NCAs can be systematically tuned by changing the diameter (D) of the binding site defined by e-beam lithography. The cluster size distribution and average cluster size n as a function of the binding size D for arrays with fixed edge-to-edge separation of Λ = 200 nm are given in Figure 5a. Individual 40 nm gold nanoparticles are the predominant building block for a site diameter of D = 50 nm. However, the number of particles on the binding sites grows with D. The average cluster size n increases steadily from n = 1.3 for D = 50 nm to n = 4.4 for D = 120 nm and then jumps to n = 19.1 for D = 200 nm (see Figure 5a).

The peak wavelengths of the scattering spectra of the NCAs analyzed in Figure 5a are plotted as a function of n in Figure 5b. The original spectra are given in the Figure 5b inset. The peak wavelength (λ_{res}) strongly red shifts from 558 nm for n = 1.3 to 670 nm for n = 4.4. However, further increases of the cluster size beyond n = 4.4 lead to only small additional red shifts of the scattering band. The peak wavelength increases by only 9 nm to λ_{res} = 679 between n = 4.4 and n = 19.1.

The strong red shift of the spectral response with increasing degree of particle clustering is a direct consequence of near-field coupling between the particles in the clusters, driven by the increasing number of interstitial junction plasmons as n increases. Plasmon hybridization[55] between adjacent particle plasmons leads to coupled cluster resonances that are energetically stabilized with respect to the isolated particle plasmons. Figure 5b shows that this stabilization effect saturates in larger clusters. The major portion of the energy stabilization is reached for an average cluster size of n = 4.4. A further increase in the size of the clusters results in only a small additional shift of their plasmon resonance wavelength.

The nearly constant plasmon resonance frequency for clusters with $n \geq 4$ may be understood from simple geometric considerations. A close inspection of the SEM images of the fabricated NCAs reveals that clusters with n = 4 preferentially assume a rhombohedral geometry where the interparticle distances are minimized (see Figure 2f). Four gold nanoparticles at the edges of a rhombus form the unit cell of a monolayer of hexagonal closed packed spheres. This highly symmetric arrangement enables the particles to minimize the total interparticle separation resulting in very efficient plasmon coupling. The fact that an increase in the average cluster size beyond n = 4 does not lead to substantial additional spectral shifts in regular arrays therefore implies that the coupling in the larger clusters is dominated by interparticle coupling between nearest neighbors in the unit cell.

In three-dimensional clusters, additional interactions between particles along the third spatial axis (out-of-plane) can shift the plasmon resonance further into the red than observed here for two-dimensional clusters. Some of the fabricated NCAs contain contaminations with larger three-dimensional agglomerates due to imperfections during the fabrication process (see Figure S2 in the Supporting Information). Shoulders at wavelengths >800 nm in the scattering spectra shown in Figure 5b are ascribed to these three-dimensional clusters and fractal particle assemblies. The occasional contamination of the fabricated NCAs does, however, not influence the observed global trends: the peak wavelength red shifts in the interval $1 < n < 4$ and converges to its maximum at $n \approx 4$.

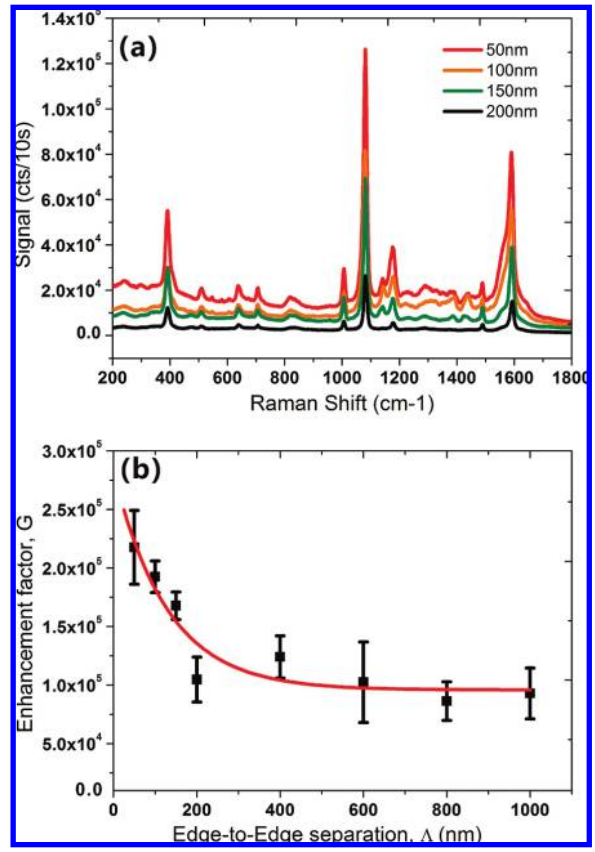

Figure 6. (a) SERS spectra of a monolayer of pMA on NCAs with an average cluster size of n = 19.1 (D = 200 nm) as function of the edge-to-edge separation Λ (see legend). The pump power is 1.8 mW and the integration time is 10 s. (b) Approximate SERS enhancement factors G as the function of the edge-to-edge separation Λ.

SERS Performance of Nanoparticle Cluster Arrays. Fabrication procedures that provide spatial control on the nanoscale are instrumental in developing SERS substrates according to rational design criteria. Our motivation for assembling arrays of clusters of nearly touching gold nanoparticles at defined locations is to reproducibly create hot spots with high surface density to generate SERS substrates with large enhancement factors and improved enhancement reproducibility. The spectral characterization of the fabricated cluster arrays has already indicated the existence of

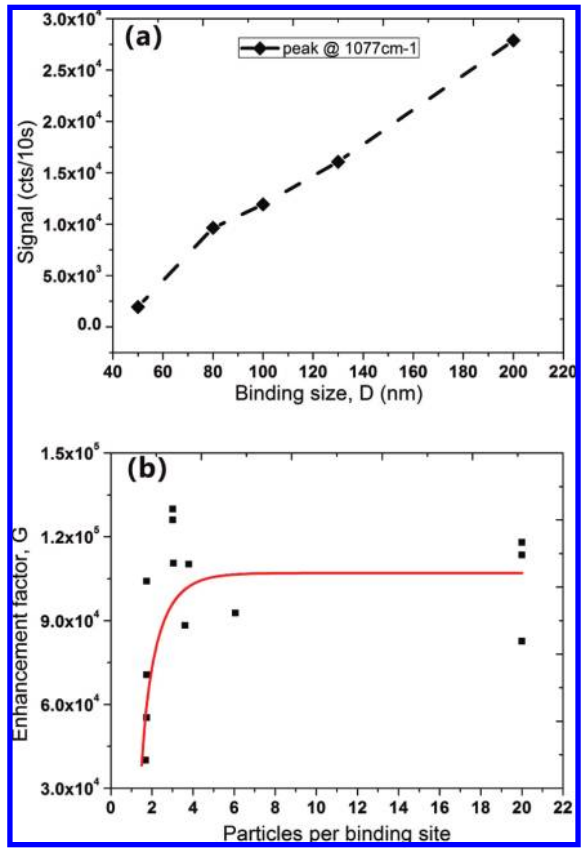

Figure 7. (a) SERS intensity of the 1077 cm^{-1} transition from a monolayer of pMA on NCAs with fixed cluster edge-to-edge separations Λ as function of the e-beam defined cluster binding size *D*. The pump power is 1.8 mW, and the acquisition time is 10 s. (b) Average SERS enhancement factor *G* as a function of the average cluster size (Λ = 200 nm).

both interparticle and intercluster plasmon coupling in NCAs. In order to be able to utilize the interplay of electromagnetic interactions between individual nanoparticles in the clusters and between clusters, it is important to characterize the influence of the array specific geometry parameters Λ and *n* on the relative Raman intensities. All SERS spectra in this study were excited at 785 nm, an experimentally convenient laser excitation wavelength. This wavelength has been shown to minimize autofluorescence from biological samples.[28]

Influence of the Cluster Edge-to-Edge Separation (Λ) on the SERS Signal. Following other SERS studies,[5] *para*-mercaptoaniline (pMA) was used here as a test analyte to quantify the influence of Λ on the NCA Raman signal enhancement. To optimize the SERS performance of the substrates, the SERS signal dependence on pump power *P* (*P* = 0.4−7.3 mW) and data acquisition time *t* (*t* = 10−60 s) was first investigated (see Figure S3 in the Supporting Information). The pMA SERS intensity on a Λ = 200 nm, *D* = 200 nm NCA was found to be linearly dependent on *P* and *t* in the investigated ranges. SERS substrates with excellent signal-to-noise are obtained with 10 s of data collection and *P* = 1.8 mW. All SERS measurements subsequently reported were performed with these acquisition parameters unless otherwise stated.

Figure 6a contains pMA SERS spectra from NCAs with different values of Λ but with fixed nanoparticle binding sizes (*D* = 200 nm). Two effects contribute to the strong increase of the SERS intensity with decreasing edge-to-edge separation. First, the density of the nanoparticle clusters and therefore the total SERS active area in the scattering volume increases with decreasing Λ. Second, the NCA scattering spectra as a function of intercluster separation (Figure 4) revealed that for short edge-to-edge separations (Λ < 200 nm) additional intercluster coupling further enhances the local |*E*|-field. Such a local field enhancement effect is evident from a comparison of SERS enhancement factors, *G*, as function of Λ. The absolute values of these enhancement factors are only approximate since the surface coverage with pMA, the accessible surface area of the clusters, the contribution of the gold substrate, as well as the number of molecules in the reference sample have to be estimated (see Methods section). Nevertheless, they facilitate a quantitative comparison of the relative SERS performances of samples with different filling fractions (*i.e.*, different Λ), prepared under otherwise identical conditions. The approximate enhancement factors obtained for the 1077 cm^{-1} band of pMA on NCAs with constant binding site diameter (*D* = 200 nm) are plotted as function of Λ in Figure 6b.

The measured SERS enhancement decreases from 2.2 × 10^5 for Λ = 50 nm to 1 × 10^5 for Λ = 200 nm. The SERS enhancement is essentially independent of Λ for larger edge-to-edge separations. The gain in *G* at short intercluster separations is in agreement with the observed spectral red shift of the plasmon resonance and is consistent with increasing near-field interactions between the clusters for Λ < 200 nm. The near-field intercluster interactions increase the SERS enhancement generated by individual clusters by a factor of ~2 with respect to the isolated clusters at the smallest Λ tested in this study. This observation further corroborates that plasmon coupling in NCAs occurs on two relevant length scales: *interparticle* in the clusters and *intercluster* in the arrays.

Influence of Cluster Size on the SERS Signal. The SERS enhancement as a function of the binding size diameter *D* and thus the average cluster size, *n*, in NCAs with fixed edge-to-edge separation Λ have also been investigated.

In Figure 7a, the SERS intensities of the pMA 1077 cm^{-1} transition of NCAs with five different *D* values (50, 80, 100, 130, 200 nm) and fixed edge-to-edge separation (Λ = 200 nm) are compared. All of these nanoparticle cluster arrays were fabricated on the same chip to minimize intensity effects due to pMA concentration or pump power variability. The recorded signal intensity increases nearly linearly with *D*. *A priori*, it is unclear how much a potential cluster size dependence of

the SERS enhancement contributes to the signal intensity gain. The influence of D on the SERS enhancement was therefore estimated by calculating the SERS enhancement factors G as function of D (see Figure 7b). The general trend in Figure 7b indicates that G does not continuously increase with cluster size n but converges against a maximum enhancement at $n \approx 3-4$. In the case of NCAs with fixed $\Lambda = 200$ nm, a maximum enhancement factor of $G \approx 1 \times 10^5$ is reached. This behavior corroborates the trends observed for the plasmon resonance wavelength.

The constant scattering maximum wavelength for $n \geq 4$ in Figure 5 was rationalized by the maximization of the interparticle near-field interactions in compact cluster geometries. In addition, in clusters of three or four particles with triangular or rhombal cluster geometry, all particles can be arranged in a "first coordination shell" around a central cavity. Analyte molecules located in this space can potentially experience very high local fields leading to strong SERS enhancements, highlighting the value of the first interstitial coordination shell for SERS signal enhancement.

Benchmark NCAs with Competing SERS Substrates Using *para*-mercaptoaniline (pMA) as Test Substance. We evaluated the performance of NCAs by direct comparison with two commonly used SERS substrates: nonpatterned 40 nm gold nanoparticle films[56] and periodic two-dimensional arrays of gold nanodisc arrays.[19] The nonpatterned colloid films were conveniently generated on the same substrate adjacent to the nanoparticle cluster arrays by simply removing the photoresist from a large area in the vicinity of the surface pattern during the e-beam writing step. All subsequent processing steps were identical to the procedures described above for the production of the nanoparticle cluster arrays. The nanodisc arrays were fabricated on a 10 nm thin gold film following standard procedures. In short, a PMMA mask was generated on top of a gold-coated glass slide by direct writing e-beam lithography with subsequent development. Then a 40 nm thick gold layer was thermally evaporated onto the patterned surface, and the PMMA mask was removed in a final lift-off step releasing the regular gold nanodisc pattern. The NCAs used for the benchmarking had an edge-to-edge separation of $\Lambda = 200$ nm and a cluster binding size of $D = 200$ nm. The nanofabricated nanodisc arrays had the same edge-to-edge distance and total diameter as the NCAs.

The relative SERS performance of these three different substrates was evaluated in direct comparison under identical conditions. The Raman enhancement (G) factors at 785 nm for the 1077 cm^{-1} mode of pMA and corresponding representative SEM images of the investigated substrates are summarized in Figure 8. These values correspond to 12 measurements from three different substrates for each substrate type. The NCA substrates yielded the overall largest G values ($\sim 1.1 \times 10^5$), followed by the nonpatterned nanoparticle film

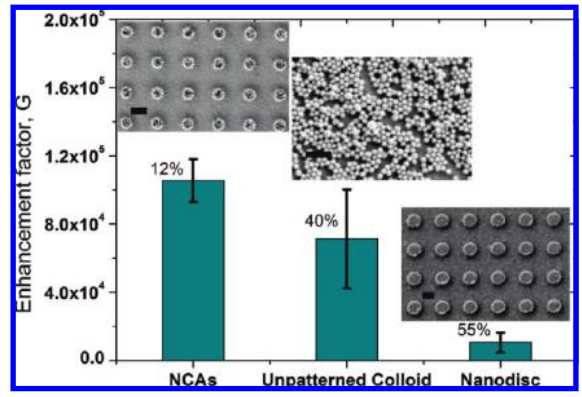

Figure 8. Comparison of approximate SERS enhancement factors G of ($\Lambda = 200$ nm, $D = 200$ nm) NCAs, nonpatterned gold nanoparticle films, and nanodisc arrays (edge-to-edge distance = 200 nm, disk diameter = 200 nm, disk height = 40 nm). The error bars indicate the standard deviation from 12 independent measurements on four substrates. The standard deviation as percentage of the mean and SEM images of all three substrates are included. Scale bars in all SEM images denote 200 nm.

($\sim 7.0 \times 10^4$). The nanodisc array exhibited the smallest G values ($\sim 1.0 \times 10^4$). NCAs with $\Lambda = 50$ nm, $D = 200$ nm yielded the maximal enhancement factor of $G = 2.2 \times 10^5$ for the substrates prepared for this study (see Figure 6). These values fall within the typical SERS enhancement range of gold island films[57] and are comparable with those obtained with other engineered SERS substrates such as gold nanohole arrays.[11] Although enhancement factors up to 1×10^8 have been observed in some cases for e-beam patterned gold nanodisc arrays fabricated on a gold film,[53] the NCAs are found to provide a significantly higher ($\sim$1 order of magnitude) Raman signal enhancement than the corresponding nanodisc arrays, at least for pMA excited at 785 nm.

The observation that the NCAs provide a stronger SERS signal enhancement than smooth nanodisc arrays with identical array geometry is readily ascribed to the fact that the NCAs have a much higher degree of roughness than the nanodiscs due to crevices, holes, and junctions between the nanoparticles in the clusters. The incident field can be effectively localized in these nanoroughened structures, leading to overall higher enhancement factors. Nanoscale roughness can, however, not account for the fact that the ensemble-averaged SERS enhancement factors for NCAs are also slightly higher than those of the nonpatterned gold nanoparticle films which also contain nanoparticle clusters. On the basis of the observed dependencies of the ensemble-averaged G factors on Λ and n, we propose the following model to account for the observed differences between patterned and nonpatterned colloid substrates. The SERS enhancement factor of individual two-dimensional nanoparticle clusters saturates at around $n \approx 4$. In an array of patterned clusters, the total SERS enhancement of the individual clusters can be further increased through cumulative electrodynamic

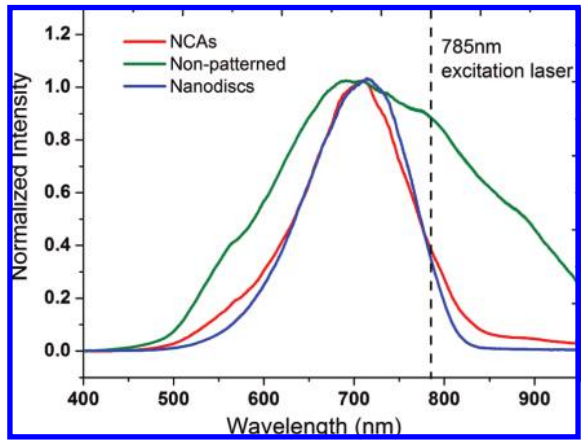

Figure 9. Rayleigh scattering spectra of (D = 200 nm, Λ = 200 nm) NCAs, nonpatterned nanoparticle films and periodic disk array (disk diameter = 200 nm, edge-to-edge separation = 200 nm). The dashed line indicates the wavelength of the SERS excitation laser (785 nm).

interactions occurring on two different length scales. On the length scale of a few tens of nanometers (intercluster length scale), the cluster plasmons couple and provide a first stage of strong enhancement of the incident electric field. This enhanced field is then further increased by the intracluster coupling between the individual particles of the clusters. The phenomenon therefore consists of a sequential enhancement similar to the effects observed in RF Yagi antennas[58] or optical nanolenses.[59]

The Raman signal enhancement generated by plasmonic nanostructures can be maximized by matching the excitation wavelength with the dipolar resonances of the corresponding substrates.[34] It is therefore interesting to investigate the spectral match of the excitation wavelength with the scattering resonances of the investigated substrates, which in case of the NCAs are expected to be dominated by the dipolar plasmon resonances. Figure 9 shows the normalized spectra of the investigated NCAs, smooth gold nanodisc arrays, and nonpatterned colloid films. Whereas NCAs and nanodisc arrays show well-defined plasmon resonances at around ~700 nm with a full width at half-maximum (fwhm) extending from 630 to 780 nm, the nonpatterned colloid film shows a much broader scattering spectrum with fwhm between 580 and 880 nm. We ascribe this spectral broadening to the wide distribution of cluster sizes including three-dimensional and fractal aggregates in the nonpatterned colloid film.

The measured relative Rayleigh scattering intensities for NCAs and nanodisc arrays have decreased to ~30% of their peak intensity value at the SERS excitation wavelength of 785 nm. In contrast, for the nonpatterned colloid substrate, the scattering cross section is close to its peak value at the 785 nm SERS excitation wavelength. The detuning between 785 nm Raman excitation wavelength and the resonance scattering maxima evident in Figure 9 suggests that—unlike the nonpatterned colloid films—the enhancement factors of NCAs could be further increased by improving the match between the plasmon resonance wavelength maximum and Raman excitation laser wavelength.

Another important SERS performance characteristic, in addition to the signal enhancement, is the reproducibility of the enhancement factors generated by different SERS substrates. The enhancement factor (G) reproducibility is characterized here by the coefficient of variability, that is, the standard deviation of G values given by 12 independent measurements on three different substrates, expressed as a percentage of the mean G value for each substrate type. These variability coefficients are given in Figure 8. As evident from this measure for G reproducibility, the variations of the NCAs enhancement (12%) is much smaller than that observed on either the nonpatterned colloid substrate (40%) or the nanodiscs (55%). Despite the nanodiscs' well-defined structure, the overall low SERS signal enhancement generated by these substrates leads to a large coefficient of variability in their G values. Thus both in terms of absolute enhancement and repeatability, the NCAs outperform the other two substrate types tested here.

SERS Bacterial Detection and Identification Using NCAs. The SERS performance of NCAs makes them potentially useful candidates for complex sensing applications such as whole cell fingerprinting. There is currently significant interest in developing SERS for the rapid characterization and identification of bacterial pathogens.[27,28,44,60,61] Due to the distance dependence of the field enhancement, SERS selectively probes the molecular components of the outer layer of bacterial cells where chemical distinctions appear to be the greatest, thus enhancing specificity, and may therefore be a promising tool for bacterial diagnostics.[28,44] The successful application of SERS for this analytical application requires substrates that can provide strong and reproducible enhancements for these organisms at the single cell level and have a storable shelf life in the 6−12 month range.

For bacterial samples, the surface morphology and the binding affinity to the substrate are extremely important and can influence both the detected vibrational bands and the total signal intensities of the SERS signatures. Not all SERS active substrates provide SERS spectra of whole bacterial cells. Only if a bacterial cell can effectively attach to the surface such that characteristic surface moieties are near SERS active sites will a strong Raman signal be observed.

In order to test the ability of the NCAs, the nonpatterned colloid films, and the nanodiscs to act as effective substrates for the observation of SERS spectra of vegetative bacterial cells, suspensions of three different bacterial species (*S. aureus*, *E. coli*, and *B. cereus*) were placed on these substrates and SERS spectra excited at 785 nm (4.3 mW power, 10 s integration time)

were acquired. All bacterial cells in the Raman illuminated area of 2.5 μm × 25 μm contributed to the recorded SERS spectra; considering the average sizes of the bacterial cells and the high surface coverage with bacteria (see Figure S4 in the Supporting Information), we estimate that on average 12 (*B. cereus*), 80 (*S. aureus*), or 62 (*E. coli*) cells occupy this sample region.

Only very weak bacterial SERS spectra could be observed on the smooth nanodisc arrays (edge-to-edge distance = 200 nm, disk diameter = 200 nm, disk height = 40 nm). However, both patterned (NCA) and nonpatterned colloid substrates provided quantifiable SERS signals. Representative SERS spectra (single scan) of *S. aureus*, *E. coli*, and *B. cereus* obtained from NCAs (Λ = 200 nm, D = 200 nm) and nonpatterned colloid substrates are shown in Figure 10. The nonpatterned gold nanoparticle substrates were located on the same chip in close vicinity to the nanoparticle cluster array to ensure that these two samples were always measured under identical experimental conditions. As seen in Figure 10, SERS spectra of bacteria are stronger on the NCA substrates than on the nonpatterned colloid films. Furthermore, in contrast to the NCA bacterial spectra, the bacterial SERS signal intensities exhibited strong variations at different positions on the nonpatterned substrates.

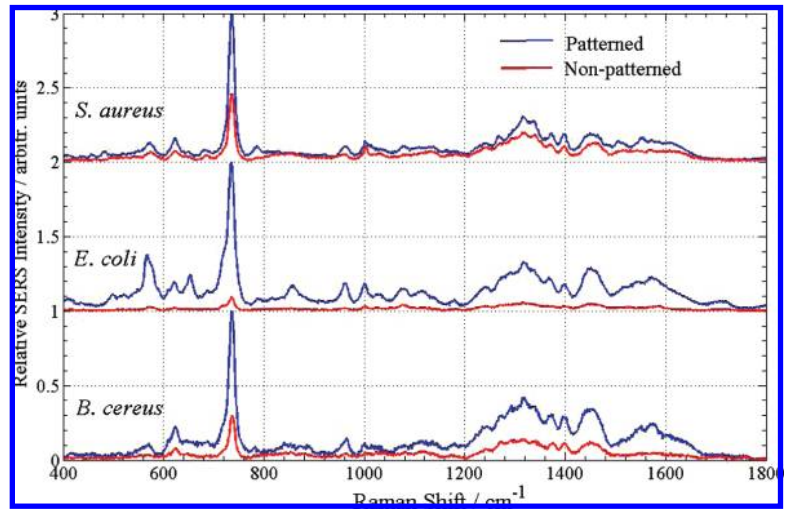

Figure 10. SERS spectra of *Staphylococcus aureus*, *Escherichia coli*, and *Bacillus cereus* recorded on NCAs (blue) and on nonpatterned gold nanoparticle films (red).

The bacterial SERS spectra share many common spectral features as evident in Figure 10 and have been discussed previously.[28,44,61] Identification of the chemical species responsible for the vibrational bands in the SERS spectra of bacteria has not yet been achieved and is beyond the scope of this current report. However, the unique SERS vibrational signatures provide the basis for a rapid bacterial identification methodology when combined with multivariate library searching techniques.

The ability of NCAs to be used for bacterial diagnostics is demonstrated in Figure 11. It has been shown previously how a principal component analysis (PCA) based on the sign of the second derivative of the SERS spectra provides improved specificity for the identification of bacterial species and strains.[44] The SERS spectra are thus reduced to a series of zeroes and ones (*i.e.*, barcodes) as input for unsupervised clustering algorithms such as PCA or consequent supervised methods such as discriminant function analysis, hierachial cluster analysis, or neural network techniques. Here the specificity of these SERS-based signatures on NCAs is shown by the results of a discriminant function analysis (DFA) based on the barcode reduced SERS spectra of *S. aureus*, *E. coli*, and *B. cereus*. The discriminant functions are linear combinations of the first four PCs which capture 98% of the variance of this 30 spectra data set.

As seen in the DF2 *versus* DF1 plot in Figure 11, the SERS signatures of *B. cereus*, *E. coli*, and *S. aureus* obtained on the NCAs are well-separated, forming nonoverlapped regions. The rings in each of the cluster regions correspond to two-dimensional standard deviations centered on the mean for each species cluster. The large separations, measured in terms of standard deviations, indicate that the NCAs enable a spectral signature capable of bacterial identification. This finding is important because not all SERS substrates yield strong reproducible spectra of bacterial cells although they may result in strong SERS spectra of some molecular analytes. While the presented data are preliminary with only three bacterial species tested, the demonstrated bacterial identification capability is nevertheless an important figure of merit for the evaluation of the NCAs as potential SERS substrates for bacterial pathogen identification. Work is currently ongoing in our laboratories to determine the best performing SERS substrates for this purpose based on the criteria of Raman enhancement strength, spectral reproducibility, substrate storage lifetime, and commercial scalability.

CONCLUSIONS

We fabricated nanoparticle cluster arrays (NCAs) by combining top-down nanofabrication and bottom-up self-assembly procedures in a template-guided self-assembly process. This approach provides control over the size of the particle clusters and their spatial location on the nanoscale. We used this process to fabricate regular arrays of 40 nm gold nanoparticle clusters of defined cluster size n and cluster edge-to-edge separation Λ over several hundred square microns. The photonic-plasmonic scattering resonances of the arrays as a function of n and Λ were characterized. The spectra are dominated by the ensemble resonance of the gold film supported nanoparticle clusters at large cluster separations. For NCAs with short intercluster separations, $\Lambda < 200$ nm, we also observe an additional short wavelength band which we ascribe to light

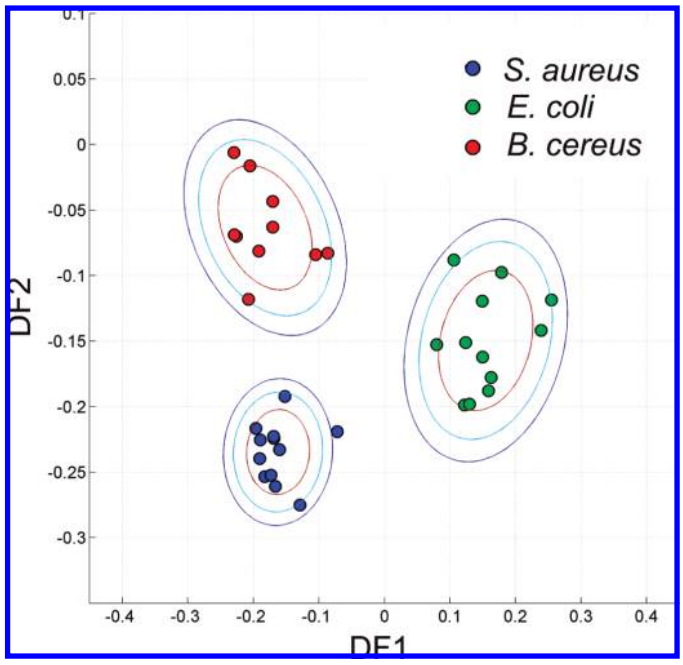

Figure 11. DFA plot for the SERS spectra of three different bacteria species: *B. cereus*, *E. coli*, and *S. aureus* acquired on NCAs (40 nm gold nanoparticles, $D = 200$ nm, $\Lambda = 200$ nm). Each ring centered on the resulting three clusters corresponds to a two-dimensional standard deviation from the cluster mean. The 30 input SERS signatures cluster in well-separated areas, demonstrating the potential use of these substrates for SERS-based bacterial diagnostics.

diffraction from the NCAs acting as transmission grating for the incident light. A systematic variation of Λ revealed that the plasmon resonance peak red shifts with decreasing Λ for edge-to-edge separations $\Lambda \leq 200$ nm, indicating additional intercluster near-field interactions. The red shift of the plasmon resonance is accompanied by an increase in the SERS enhancement for $\Lambda \leq 200$ nm. This observation confirms that electrodynamic interactions between the clusters can further increase the Raman signal intensity generated by individual isolated clusters, and we conclude that the net enhancement is the result of a multiscale field enhancement in NCAs. Next to the edge-to-edge separation, the SERS signal enhancement also depends on the cluster size n, and we investigated the optical response and the SERS enhancement of NCAs as a function of n. The cluster resonances of the arrays strongly red shift with increasing cluster size n up to $n \approx 4$. We did not observe a further significant increase in the enhancement for larger two-dimensional nanoparticle clusters. Similarly, the Raman signal enhancement shows a significant increase with growing cluster size for small cluster sizes $n \leq 4$ but remains essentially constant for larger cluster sizes. This behavior suggests that, for $n = 4$, cluster structures are accessible which enable very efficient plasmon coupling between all particles of the clusters. We find that one of the preferred structures for $n = 4$ is the rhombus which is the unit cell of a two-dimensional close packing. The size dependency of the SERS enhancement indicates a dominance of the interstitial first shell in the Raman signal amplification.

Overall, our studies revealed that NCAs can be used to engineer SERS substrates whose spectral and field localization properties can be controlled systematically by varying n and Λ. We benchmarked NCAs with unpatterned two-dimensional gold nanoparticle substrates and regular gold nanodisc arrays. We found that NCAs offer a good compromise between signal enhancement and substrate reproducibility. In addition, the NCAs clearly outperformed the other substrates in SERS measurements of bacteria. The NCAs provided reproducible SERS signals from different bacteria species including *Bacillus cereus*, *Escherichia coli*, and *Staphylococcus aureus* and enabled a spectroscopic discrimination of these samples through SERS in combination with multivariate data analysis techniques.

Future steps for further improvement and optimization of the SERS enhancement by NCAs will involve the study of the nanoparticle composition, size, and shape as well as the geometric patterns of the arrays.

METHODS

Nanofabrication of Particle Binding Sites. We spin-coated 180 nm poly(methyl methacrylate) (PMMA) 950 on top of Au-coated (10 nm Au) glass slides. The substrates were subsequently soft-baked at 180 °C for 20 min. Periodic patterns of nanowells were then written with a Zeiss SUPRA 40VP SEM equipped with Raith beam blanker and a nanopattern generation system (NPGS). After e-beam writing, the photoresist was developed in methyl isobutyl ketone (MIBK). Periodic patterns of nanowells with interwell separations (edge-to-edge) of 50, 100, 150, 200, 400, 600, 800, and 1000 nm were generated by this procedure.

Template-Guided Self-Assembly of Gold Nanoparticle Clusters. Commercial citrate stabilized 40 nm Au particles in aqueous solution (British Biocell International) were concentrated by a factor of 10 *via* centrifugation. One hundred microliters of the concentrated gold sol was then incubated with 5 μL of a 10 mM thiol-EG_7-propionat (EG = ethyleneglycol) aqueous solution overnight at room temperature. The particles were cleaned by centrifugation and resuspended in a 10 mM phosphate buffer (pH = 8.6) containing 40 mM NaCl. The patterned gold substrates were incubated with a 1 mM aqueous solution of thiol-$(CH2)_{11}EG_7$-amine for 15 min and then washed with water. The Au particle solution was added on the top surface of the substrates and incubated for 1 h. Washing with water removed the remaining particle solution. After the samples were dried, PMMA liftoff was performed with 1-methyl-2-pyrrolidinone.

Darkfield Scattering Characterization of Periodic Cluster Arrays. Scattering images of the particle cluster arrays were recorded using an upright microscope (Olympus BX51 WI). The nanoparticle arrays were immersed in index-matching oil ($n_r = 1.5$) and illuminated with unpolarized white light from a 100 W tungsten halogen lamp using an oil darkfield condenser (NA 1.2−1.4) in transmission mode. The light scattered from the arrays was collected with a 60× oil immersion objective (NA = 0.65) and imaged using a digital camera with an active area of 620 × 580 pixels. The microscope was also equipped with a 150 mm focal length imaging spectrometer (Acton Research, InSpectrum 150) and a back-illuminated CCD detector (Hamamatsu INS-122B) that enabled the spectral analysis of the scattered light using a 150 lines/mm grating. The scattering spectra were background cor-

rected by subtraction of the scattering signal from an equal-size, unpatterned adjacent area. The scattering spectra were additionally corrected by the excitation profile of the white light source by normalizing with the scattering spectrum of an ideal white light scatterer on top of the gold film.

SERS Measurements. A Renishaw Raman microscope (model RM-2000) capable of ~2λ spatial resolution was used to observe the scattering excited by a 785 nm diode laser. The frequency calibration was set by reference to the 520 cm^{-1} silicon phonon mode. *para*-Mercaptoaniline (pMA) was used to characterize the field enhancement on the cluster arrays. The saturated aqueous pMA solution was kept on the substrate for 10 min before removing with a flow of nitrogen gas. A 50× objective (numerical aperture NA = 0.78) was used for signal collection. SERS spectra were acquired with incident laser powers in the 0.44 to 7.34 mW range and acquisition times of 10−60 s.

Calculation of Approximate SERS Enhancement Factors for *para*-Mercaptoaniline (pMA). SERS enhancement factors, *G*, were calculated following standard procedures.[5] *G* is defined here by $G = (I_{Substrate}/N_{Substrate}) \times (N_{Reference}/I_{Reference})$, where $I_{Substrate}$ is the Raman intensity of the 1077 cm^{-1} ($a1$ symmetry, C−S stretch) band resulting from a monolayer of pMA on the SERS substrate and $I_{Reference}$ is the Raman signal of the same band due to a pMA crystal. $N_{Reference}$ and $N_{Substrate}$ refer to the number of pMA molecules in a monolayer on the SERS substrate and in the focal region of the crystal, respectively. An aperture was used to confine the sample detection area to $\sigma = 2.5\ \mu m \times 25\ \mu m$. $N_{Substrate}$ was obtained as the ratio of active nanoparticle cluster array area within the detection area and the cross section of the pMA molecule ($\sigma_{pMA} = 0.3\ nm^2$). For NCAs, the active area is estimated by multiplying the number of clusters in the laser spot with the product of the average number of particles in the clusters and the surface area of one hemisphere of a 40 nm gold nanoparticle. $N_{Reference}$ was calculated assuming a confocal depth[11] of 14 μm and a density of 1.06 g/mL for solid pMA (molecular weight = 125 g/mol). For nonpatterned colloidal gold films, the surface densities of 40 nm gold particles were obtained by counting the number of particles in representative SEM images with defined dimensions. Then $N_{Substrate}$ was calculated using the same assumptions as in the case of the NCAs. In the case of smooth nanodisc arrays, $N_{Substrate}$ was determined as the ratio of active area (number of discs in the detection area multiplied by the exposed disk surface area) and σ_{pMA}.

Bacteria Growth and Sample Preparation. Gram-negative bacteria *E. coli* (ATCC #12435) and Gram-positive bacteria *B. cereus* (ATCC #14579) and *S. aureus* (ATCC #25904) were grown in 15−20 mL of LB (Sigma) for ~5 h at 37 °C until they reached an OD600 = ~0.6. About 4 mL of each culture solution was washed, centrifuged, and vortexed four times with Millipore water. Finally, the pellet was suspended in 0.25 mL of water. About 1 μL of the bacteria suspension was placed on the cluster arrays, and after the water had evaporated (~2 min), the samples were transferred into the Raman microscope to record SERS spectra.

Acknowledgment. This work was supported by the Department of Defense under ARL Cooperative Agreement No. W91NF-06-2-0040. We would like to thank Kebin Fan from the Zhang laboratory at Boston University for assistance in producing the gold nanodisc arrays, and Ishan Patel for assistance in performing PC-DFA with Matlab.

Supporting Information Available: Figures S1−S4. This material is available free of charge *via* the Internet at http://pubs.acs.org.

REFERENCES AND NOTES

1. van Duyne, R. P.; Jeanmaire, D. L. Surface Raman Spectroelectochemistry: Part1. Heterocyclic, Aromatic, and Aliphatic Amines Adsorbed on the Anodized Silver Electrode. *J. Electroanal. Chem.* **1977**, *84*, 1–20.
2. Moskovits, M. Surface-Enhanced Spectroscopy. *Rev. Mod. Phys.* **1985**, *57*, 783–826.
3. Creighton, J. A.; Blatchford, C. G.; Albrecht, M. G. Plasma Resonance Enhancement of Raman-Scattering by Pyridine Adsorbed on Silver or Gold Sol Particles of Size Comparable to the Excitation Wavelength. *J. Chem. Soc., Faraday Trans. 2* **1979**, *75*, 790–798.
4. Genov, D. A.; Shalaev, V. M.; Sarychev, A. K. Surface Plasmon Excitation and Correlation-Induced Localization-Delocalization Transition in Semicontinuous Metal Films. *Phys. Rev. B* **2005**, *72*, 113102.
5. Jackson, J. B.; Halas, N. J. Surface-Enhanced Raman Scattering on Tunable Plasmonic Nanoparticle Substrates. *Proc. Natl. Acad. Sci. U.S.A.* **2004**, *101*, 17930–17935.
6. Murphy, C. J.; San, T. K.; Gole, A. M.; Orendorff, C. J.; Gao, J. X.; Gou, L.; Hunyadi, S. E.; Li, T. Anisotropic Metal Nanoparticles: Synthesis, Assembly, and Optical Applications. *J. Phys. Chem. B* **2005**, *109*, 13857–13870.
7. Liao, P. F.; Bergman, J. G.; Chemla, D. S.; Wokaun, A.; Melngailis, J.; Hawryluk, A. M.; Economou, N. P. Surface-Enhanced Raman-Scattering from Microlithographic Silver Particle Surfaces. *Chem. Phys. Lett.* **1981**, *82*, 355–359.
8. Chen, C. Y.; Burstein, E. Giant Raman-Scattering by Molecules at Metal-Island Films. *Phys. Rev. Lett.* **1980**, *45*, 1287–1291.
9. Dick, L. A.; McFarland, A. D.; Haynes, C. L.; Van Duyne, R. P. Metal Film over Nanosphere (MFON) Electrodes for Surface-Enhanced Raman Spectroscopy (SERS): Improvements in Surface Nanostructure Stability and Suppression of Irreversible Loss. *J. Phys. Chem. B* **2002**, *106*, 853–860.
10. Bernard, S.; Felidj, N.; Truong, S.; Peretti, P.; Levi, G.; Aubard, J. Study of Langmuir−Blodgett Phospholipidic Films Deposited on Surface Enhanced Raman Scattering Active Gold Nanoparticle Monolayers. *Biopolymers* **2002**, *67*, 314–318.
11. Yu, Q. M.; Guan, P.; Qin, D.; Golden, G.; Wallace, P. M. Inverted Size-Dependence of Surface-Enhanced Raman Scattering on Gold Nanohole and Nanodisk Arrays. *Nano Lett.* **2008**, *8*, 1923–1928.
12. Haynes, C. L.; McFarland, A. D.; Zhao, L. L.; Van Duyne, R. P.; Schatz, G. C.; Gunnarsson, L.; Prikulis, J.; Kasemo, B.; Kall, M. Nanoparticle Optics: The Importance of Radiative Dipole Coupling in Two-Dimensional Nanoparticle Arrays. *J. Phys. Chem. B* **2003**, *107*, 7337–7342.
13. Felidj, N.; Laurent, G.; Aubard, J.; Levi, G.; Hohenau, A.; Krenn, J. R.; Aussenegg, F. R. Grating-Induced Plasmon Mode in Gold Nanoparticle Arrays. *J. Chem. Phys.* **2005**, *123*, 221103.
14. Gunnarsson, L.; Bjerneld, E. J.; Xu, H.; Petronis, S.; Kasemo, B.; Kall, M. Interparticle Coupling Effects in Nanofabricated Substrates for Surface-Enhanced Raman Scattering. *Appl. Phys. Lett.* **2001**, *78*, 802–804.
15. Grand, J.; de la Chapelle, M. L.; Bijeon, J. L.; Adam, P. M.; Vial, A.; Royer, P. Role of Localized Surface Plasmons in Surface-Enhanced Raman Scattering of Shape-Controlled Metallic Particles in Regular Arrays. *Phys. Rev. B* **2005**, *72*, 033407.
16. De Jesus, M. A.; Giesfeldt, K. S.; Oran, J. M.; Abu-Hatab, N. A.; Lavrik, N. V.; Sepaniak, M. J. Nanofabrication of Densely Packed Metal-Polymer Arrays for Surface-Enhanced Raman Spectrometry. *Appl. Spectrosc.* **2005**, *59*, 1501–1508.
17. Hicks, E. M.; Zou, S. L.; Schatz, G. C.; Spears, K. G.; Van Duyne, R. P.; Gunnarsson, L.; Rindzevicius, T.; Kasemo, B.; Kall, M. Controlling Plasmon Line Shapes through Diffractive Coupling in Linear Arrays of Cylindrical Nanoparticles Fabricated by Electron Beam Lithography. *Nano Lett.* **2005**, *5*, 1065–1070.
18. Zhao, L. L.; Kelly, K. L.; Schatz, G. C. The Extinction Spectra of Silver Nanoparticle Arrays: Influence of Array Structure on Plasmon Resonance Wavelength and Width. *J. Phys. Chem. B* **2003**, *107*, 7343–7350.
19. Bouhelier, A.; Bachelot, R.; Im, J. S.; Wiederrecht, G. P.; Lerondel, G.; Kostcheev, S.; Royer, P. Electromagnetic Interactions in Plasmonic Nanoparticle Arrays. *J. Phys. Chem. B* **2005**, *109*, 3195–3198.
20. Lamprecht, B.; Schider, G.; Lechner, R. T.; Ditlbacher, H.; Krenn, J. R.; Leitner, A.; Aussenegg, F. R. Metal Nanoparticle Gratings: Influence of Dipolar Particle Interaction on the Plasmon Resonance. *Phys. Rev. Lett.* **2000**, *84*, 4721–4724.

21. Gopinath, A.; Boriskina, S. V.; Reinhard, B. M.; Dal Negro, L. Deterministic Aperiodic Arrays of Metal Nanoparticles for Surface Enhanced Raman Scattering (SERS). *Opt. Express* **2009**, *17*, 3741.
22. Shalaev, V. M.; Botet, R.; Tsai, D. P.; Kovacs, J.; Moskovits, M. Fractals—Localization of Dipole Excitations and Giant Optical Polarizabilities. *Physica A* **1994**, *207*, 197–207.
23. Stockman, M. I.; Shalaev, V. M.; Moskovits, M.; Botet, R.; George, T. F. Enhanced Raman-Scattering by Fractal Clusters—Scale-Invariant Theory. *Phys. Rev. B* **1992**, *46*, 2821–2830.
24. Christensen, K.; Moloney, N. R. *Complexity and Criticality*; Imperial College Press: London, 2005.
25. Nie, S. M.; Emery, S. R. Probing Single Molecules and Single Nanoparticles by Surface-Enhanced Raman Scattering. *Science* **1997**, *275*, 1102–1106.
26. Kneipp, K.; Wang, Y.; Kneipp, H.; Perelman, L. T.; Itzkan, I.; Dasari, R.; Feld, M. S. Single Molecule Detection Using Surface-Enhanced Raman Scattering (SERS). *Phys. Rev. Lett.* **1997**, *78*, 1667–1670.
27. Jarvis, R. M.; Goodacre, R. Discrimination of Bacteria Using Surface-Enhanced Raman Spectroscopy. *Anal. Chem.* **2004**, *76*, 40–47.
28. Premasiri, W. R.; Moir, D. T.; Klempner, M. S.; Krieger, N.; Jones, G.; Ziegler, L. D. Characterization of the Surface Enhanced Raman Scattering (SERS) of Bacteria. *J. Phys. Chem. B* **2005**, *109*, 312–320.
29. Jarvis, R. M.; Brooker, A.; Goodacre, R. Surface-Enhanced Raman Scattering for the Rapid Discrimination of Bacteria. *Faraday Discuss.* **2006**, *132*, 281–292.
30. Gopinath, A.; Boriskina, S. V.; Feng, N. N.; Reinhard, B. M.; Dal Negro, L. Photonic-Plasmonic Scattering Resonances in Deterministic Aperiodic Structures. *Nano Lett.* **2008**, *8*, 2423–2431.
31. Henzie, J.; Lee, M. H.; Odom, T. W. Multiscale Patterning of Plasmonic Metamaterials. *Nat. Nanotechnol.* **2007**, *2*, 549–554.
32. Meier, M.; Wokaun, A.; Liao, P. F. Enhanced Fields on Rough Surfaces—Dipolar Interactions among Particles of Sizes Exceeding the Rayleigh Limit. *J. Opt. Soc. Am. B* **1985**, *2*, 931–949.
33. Xu, H. X.; Aizpurua, J.; Kall, M.; Apell, P. Electromagnetic Contributions to Single-Molecule Sensitivity in Surface-Enhanced Raman Scattering. *Phys. Rev. E* **2000**, *62*, 4318–4324.
34. Hao, E.; Schatz, G. C. Electromagnetic Fields around Silver Nanoparticles and Dimers. *J. Chem. Phys.* **2004**, *120*, 357–366.
35. Jiang, J.; Bosnick, K.; Maillard, M.; Brus, L. Single Molecule Raman Spectroscopy at the Junctions of Large Ag Nanocrystals. *J. Phys. Chem. B* **2003**, *107*, 9964–9972.
36. Michaels, A. M.; Jiang, J.; Brus, L. Ag Nanocrystal Junctions as the Site for Surface-Enhanced Raman Scattering of Single Rhodamine 6G Molecules. *J. Phys. Chem. B* **2000**, *104*, 11965–11971.
37. Jain, P. K.; Huang, W. Y.; El-Sayed, M. A. On the Universal Scaling Behavior of the Distance Decay of Plasmon Coupling in Metal Nanoparticle Pairs: A Plasmon Ruler Equation. *Nano Lett.* **2007**, *7*, 2080–2088.
38. Su, K. H.; Wei, Q. H.; Zhang, X.; Mock, J. J.; Smith, D. R.; Schultz, S. Interparticle Coupling Effects on Plasmon Resonances of Nanogold Particles. *Nano Lett.* **2003**, *3*, 1087–1090.
39. Reinhard, B. M.; Siu, M.; Agarwal, H.; Alivisatos, A. P.; Liphardt, J. Calibration of Dynamic Molecular Rule Based on Plasmon Coupling between Gold Nanoparticles. *Nano Lett.* **2005**, *5*, 2246–2252.
40. Liu, S. T.; Maoz, R.; Sagiv, J. Planned Nanostructures of Colloidal Gold *via* Self-Assembly on Hierarchically Assembled Organic Bilayer Template Patterns with *In-Situ* Generated Terminal Amino Functionality. *Nano Lett.* **2004**, *4*, 845–851.
41. Cui, Y.; Bjork, M. T.; Liddle, J. A.; Sonnichsen, C.; Boussert, B.; Alivisatos, A. P. Integration of Colloidal Nanocrystals into Lithographically Patterned Devices. *Nano Lett.* **2004**, *4*, 1093–1098.
42. Xia, Y. N.; Yin, Y. D.; Lu, Y.; McLellan, J. Template-Assisted Self-Assembly of Spherical Colloids into Complex and Controllable Structures. *Adv. Funct. Mater.* **2003**, *13*, 907–918.
43. Stadler, B.; Solak, H. H.; Frerker, S.; Bonroy, K.; Frederix, F.; Voros, J.; Grandin, H. M. Nanopatterning of Gold Colloids for Label-Free Biosensing. *Nanotechnology* **2007**, *18*, 155306.
44. Patel, I. S.; Premasiri, W. R.; Moir, D. T.; Ziegler, L. D. A SERS-Based Methodology for Bacterial Pathogen Identification. *J. Raman Spectrosc.* **2008**, *39*, 1660–1672.
45. Holland, W. R.; Hall, D. G. Frequency-Shifts of an Electric-Dipole Resonance near a Conducting Surface. *Phys. Rev. Lett.* **1984**, *52*, 1041–1044.
46. Mock, J. J.; Hill, R. T.; Degiron, A.; Zauscher, S.; Chilkoti, A.; Smith, D. R. Distance-Dependent Plasmon Resonant Coupling between a Gold Nanoparticle and Gold Film. *Nano Lett.* **2008**, *8*, 2245–2252.
47. Raether, H. *Surface Plasmons on Smooth and Rough Surfaces and on Gratings*; Springer: Berlin, 1988; Vol. 111.
48. Felidj, N.; Aubard, J.; Levi, G.; Krenn, J. R.; Schider, G.; Leitner, A.; Aussenegg, F. R. Enhanced Substrate-Induced Coupling in Two-Dimensional Gold Nanoparticle Arrays. *Phys. Rev. B* **2002**, *66*, 245407.
49. Sonnichsen, C.; Geier, S.; Hecker, N. E.; von Plessen, G.; Feldmann, J.; Ditlbacher, H.; Lamprecht, B.; Krenn, J. R.; Aussenegg, F. R.; Chan, V. Z. H.; Spatz, J. P.; Moller, M. Spectroscopy of Single Metallic Nanoparticles Using Total Internal Reflection Microscopy. *Appl. Phys. Lett.* **2000**, *77*, 2949–2951.
50. Sonnichsen, C.; Franzl, T.; Wilk, T.; von Plessen, G.; Feldmann, J.; Wilson, O.; Mulvaney, P. Drastic Reduction of Plasmon Damping in Gold Nanorods. *Phys. Rev. Lett.* **2002**, *88*, 077402.
51. Yang, L.; Yan, B.; Reinhard, B. M. Correlated Optical Spectroscopy and Transmission Electron Microscopy of Individual Hollow Nanoparticles and Their Dimers. *J. Phys. Chem. C* **2008**, *112*, 15989–15996.
52. Stuart, H. R.; Hall, D. G. Enhanced Dipole−Dipole Interaction between Elementary Radiators near a Surface. *Phys. Rev. Lett.* **1998**, *80*, 5663–5666.
53. Felidj, N.; Truong, S. L.; Aubard, J.; Levi, G.; Krenn, J. R.; Hohenau, A.; Leitner, A.; Aussenegg, F. R. Gold Particle Interaction in Regular Arrays Probed by Surface Enhanced Raman Scattering. *J. Chem. Phys.* **2004**, *120*, 7141–7146.
54. Kitson, S. C.; Barnes, W. L.; Sambles, J. R. Full Photonic Band Gap for Surface Modes in the Visible. *Phys. Rev. Lett.* **1996**, *77*, 2670–2673.
55. Prodan, E.; Radloff, C.; Halas, N. J.; Nordlander, P. A Hybridization Model for the Plasmon Response of Complex Nanostructures. *Science* **2003**, *302*, 419–422.
56. Zhu, Z. H.; Zhu, T.; Liu, Z. F. Raman Scattering Enhancement Contributed from Individual Gold Nanoparticles and Interparticle Coupling. *Nanotechnology* **2004**, *15*, 357–364.
57. Haynes, C. L.; McFarland, A. D.; Van Duyne, R. P. Surface-Enhanced Raman Spectroscopy. *Anal. Chem.* **2005**, *77*, 338a–346a.
58. Li, J. J.; Salandrino, A.; Engheta, N. Shaping Light Beams in the Nanometer Scale: A Yagi-Uda Nanoantenna in the Optical Domain. *Phys. Rev. B* **2007**, *76*, 245403.
59. Li, K. R.; Stockman, M. I.; Bergman, D. J. Self-Similar Chain of Metal Nanospheres as an Efficient Nanolens. *Phys. Rev. Lett.* **2003**, *91*, 227402.
60. Haynes, C. L.; Yonzon, C. R.; Zhang, X. Y.; Van Duyne, R. P. Surface-Enhanced Raman Sensors: Early History and the Development of Sensors for Quantitative Biowarfare Agent and Glucose Detection. *J. Raman Spectrosc.* **2005**, *36*, 471–484.
61. Premasiri, W. R.; Moir, D. T.; Klempner, M. S.; Ziegler, L. D. *Surface Enhanced Raman Scattering of Microorganisms*; Oxford University Press: New York, 2007.